J Mater Sci: Mater Med (2011) 22:193–200
DOI 10.1007/s10856-010-4187-1

Electrochemical behaviour and surface characterisation of Zr exposed to an SBF solution containing glycine, in view of dental implant applications

Benedetto Bozzini · Paolo Carlino · Claudio Mele

Received: 4 June 2010 / Accepted: 9 November 2010 / Published online: 24 November 2010

Abstract Zr and Ti alloys are extensively used in the biomedical field owing to their optimal mechanical properties and excellent corrosion resistance. Fully ceramic implants based on zirconia are appealing with respect to the traditional Ti-based metallic ones for several reasons, such as: (i) improved aesthetic impact, (ii) better biocompatibility and (iii) better osteointegration. Nevertheless, fully ceramic implants exhibit serious mechanical and clinical drawbacks, chiefly brittleness and impossibility of post-implant position adjustments. In this paper we propose the novel approach of using a metal-based system, consisting of metallic Zr, for the bulk of the implant and an electrochemically grown zirconia coating, ensuring contact of the ceramic with the biological environment and isolation from the underlying metal. This solution combines the outstanding mechanical properties of the metal in the bulk with the optimal biochemical properties exclusively where they are needed: at the surface. The present paper—focussed on the electrochemical behaviour of the proposed system at the implant-wound and implant-growing bone interface—reports a time-dependent electrochemical corrosion study of zirconia-coated zirconium, performed in the following ways: (i) exposure and measurements in SBF (simulating the inorganic part of human plasma, relevant to wound chemistry), (ii) exposure and measurements in SBF with added glycine (the simplest, ubiquitous amino acid found in proteins), (iii) exposure in SBF with added glycine and measurements in SBF. Electrochemical impedance spectra were measured and interpreted with the equivalent-circuit approach, yielding estimates of the time-variation of the oxide film thickness and resistance were estimated. FT-IR, Surface Raman and VIS reflectance spectroscopies were used to characterise the surface before and after the exposure to SBF solutions. Spectroelectrochemical measurements revealed an higher corrosion resistance of the oxide films formed on Zr in the presence of glycine in the SBF matrix and a smoother electrode surface.

B. Bozzini (✉) · C. Mele
Dipartimento di Ingegneria dell'Innovazione, Università del Salento, Via Monteroni, 73100 Lecce, Italy
e-mail: benedetto.bozzini@unisalento.it

P. Carlino
Dipartimento di Odontostomatologia e Chirurgia, Università di Bari, Piazza Giulio Cesare, 70124 Bari, Italy

1 Introduction

Zirconia is an appealing material for dental implants for three chief reasons: (a) better biocompatibility with respect to Ti, (b) better osteointegration, (c) aesthetic outcome, resulting from the fact that its colour is closer to that of natural enamel. Nevertheless, owing to the brittleness of zirconia, fully-ceramic implants exhibit two major drawbacks: (a) clinical cases of implant mechanical failure are much more frequent than with Ti, (b) impossibility of applying the tooth prosthesis separately from the stalk, resulting in the need of using an integral object, with serious medical and aesthetic implications, such as the probability of teeth-array misalignment, the necessity of implant dismounting, the impossibility of applying the tooth prosthesis—giving rise to the mechanical loading to the implant-bone interface—when the mechanical resistance of the stalk-bone system has reached an optimal level.

In this paper, we propose an innovative system, consisting of a bulk metallic Zr stalk with a zirconia coating. This approach allows to integrate: (i) the ideal mechanical

properties of the metal, including the possibility of applying optimised sand blasting, where they are needed—i.e. in the bulk of the implant—and (ii) the superior biochemical properties of zirconia at the interface involved in osteointegration. Of course, if the zirconia interlayer were able to ideally separate the metal from the living tissue, no biochemical differences would be found between a fully-ceramic system and the composite approach we are proposing. ZrO_2 coatings can be grown either by anodisation of Zr or by one of several available film-deposition approaches. In this paper we concentrate on ZrO_2 layers that developing by exposure to the environment, with a process similar to Ti passivation in implant environments.

Our study of the Zr/ZrO_2 system is chiefly intended to address the interfacial electrochemistry of the implant material with the evolving wound chemistry resulting from surgery: for this reason—along the lines sketched in [1] for the case of Ti implants—we chose to simulate human plasma and resorted to SBF as an adequate means. As far as corrosion of Zr and its alloys in environments of biochemical interest are concerned, limited literature information is available: below we sketch the state of the art. Titanium–zirconium alloys have been reported to show high corrosion resistance and excellent biocompatibility [2, 3]. The corrosion resistance and the ability to repassivate of the Ti–13Nb–13Zr alloy in phosphate-buffered saline containing bovine albumin solutions or foetal calf serum at different pH values was investigated for orthopaedic applications [4] and its hemocompatibility was related with surface electrochemical properties [5]. The Ti–15Zr–4Nb–2Ta–0.2Pd alloy was demonstrated to exhibit a high degree of cytocompatibility and corrosion resistance [6]. Nanocomposite films of ZrN–Ag, deposited on medical grade Ti–Al–V, showed good tribological properties in bovine serum [7]. The Ti–15Zr–4Nb–4Ta alloy revealed an excellent corrosion resistance in solutions simulating body fluids and a low metal release rate and is consequently regarded as suitable for long-term implants [8, 9] and dental prostheses [10]. PVD Zirconium nitride coatings grown onto Ti6Al4V were demonstrated to represent a viable solution to fretting corrosion problems of orthopaedic implant alloys [11]. Biocompatibility and corrosion tests in physiological NaCl solutions were performed with the pure elements employed for the fabrication of β-titanium alloys, among which zirconium [12]. Zirconium has been reported to form passivating films at room temperature [13]: the oxide films, obtained by cathodic polarization in Hank's solutions were proved to exhibit better protective properties than those grown on titanium [14]. On the basis of this information and in order to gain some fundamental understanding, we started our research on this class of novel materials with pure Zr.

2 Materials and methods

2.1 Chemicals and analytical methods

Zr (purity 99.7% from Goodfellow) in the form of rectangular foils (2×3 cm^2) and rods (diameter 8 mm) was employed. Prior to measurements, the Zr samples were pretreated by mechanical polishing with emery papers of different grades down to 1 μm.

The measurements were carried out with the following solutions.

(A) SBF: NaCl 20.2 g l^{-1}, $NaHCO_3$ 0.483 g l^{-1}, Na_2SO_4 0.104 g l^{-1}, Na_2HPO_4 0.411 g l^{-1}, KCl 0.716 g l^{-1}, $CaCl_2$ 0.433 g l^{-1}, $MgCl_2$ 0.381 g l^{-1}, pH 6.9 [15].
(B) SBF + glycine 1 g l^{-1}.

EIS experiments were performed with an AMEL 5000 potentiostat connected to a Frequency Response Analyser (Solartron SI 1250): the adopted frequency range was 65 kHz–1 MHz and the amplitude of the voltage modulation was 10 mV peak-to-peak. The measurements were performed at room temperature, using a three-electrode cell holding 75 ml of electrolyte. An Ag/AgCl reference electrode was used and all potentials are reported on the Ag/AgCl scale. The counter-electrode was a platinised Ti expanded mesh electrode of nominal area 10 cm^2. In all experiments, between subsequent EIS measurements, the samples were kept immersed in sealed vessels containing 150 ml of the relevant aerated solutions. The EIS spectra were fitted to a suitable equivalent-circuit model, described in Sect. 2.2, with the Z-view software (Scriber Associated Inc).

Surface Raman measurements were carried out with a Raman microprobe system (LabRam Jobin-Yvon) equipped with a confocal microscope, CCD detector, interferometric and holographic notch filters and 50× long-working-distance objective. A He–Ne laser provided the excitation at 633 nm and the power delivered to the sample was about 7 mW.

FT-IR measurements were carried out with a Nicolet NEXUS, equipped with an MCT-High D* detector cooled by liquid nitrogen. The beam path of the FT-IR spectrometer was continuously purged with a Parker Balston 75-52-12VDC CO_2 remover/air dryer system. The samples were located in the beam path of a VeeMax mirror system, with reflection angle set at 60°. p-polarised light was used, obtained with a ZnSe Au wire grid polarizer. The resolution of the spectrometer was set to 4 cm^{-1} and each measurement was obtained by averaging 256 spectra.

ERS measurements were carried out at 45° incidence angle with p-polarised light. The spectrometer, optics and control electronics were constructed in the Electrochemical Laboratory of the University of Salento. Solid state light

sources were employed: a set of three LEDs was used to cover the required spectral range in the VIS and UV (220–670 nm). The wavelength was selected by a grating monochromator with a spectral resolution of 7 nm. A photodiode detector was employed.

X-ray diffractometry was performed with a Ultima+Rigaku diffractometer equipped with a copper anticathode and a Bragg-Brentano goniometer. SEM micrographs were recorded with a SEM ZEISS EVO 50 XVP.

2.2 EIS models

In the interpretation of impedance data, models based on [16–21] were considered. The literature models—among the many suitable for the study of passivating materials—essentially represent the dynamic behaviour of compact single or double layers, comprising a compact and a porous part. In the case of single layer models, the capacitance of the compact layer can be used to evaluate its thickness. This model neglects the presence of the space-charge region and may result in estimation errors of the oxide film thickness. It is possible to take this factor into account—obtaining, of course, a higher dimensional space of parameters, with the resulting uncertainties in the estimate of the parameters themselves [22]—by adding an RC parallel accounting for the resistance R_{SC} (Ω cm^2) and the capacitance C_{SC} (F cm^{-2}) of the space-charge layer. On the basis of these considerations, the simplest—as well as more statistically reliable—equivalent circuit able to describe the fundamental electrochemical phenomenology highlighted in this study, resulted to be an RC parallel, with resistance R_P (Ω cm^2) and capacitance C_P (F cm^{-2}), typical of passive films. Under these assumptions, the passive film thickness d is inversely proportional to C_p [23]:

$$d = \frac{\varepsilon \cdot \varepsilon_o \cdot A}{C_P} \quad (1)$$

where ε is the relative dielectric constant of the oxide, ε_o that of vacuum and A is the nominal electrode surface area. Because—as witnessed by SEM micrographs (Sect. 3.2.1) and by the evolution of CPE parameters (Sect. 3.1)—the roughening resulting from environmental exposures studied is limited, the geometric area adequately quantifies the observable A. In the relevant case, expressing d in nm, C_P in μF and A in cm^2, it results that: $\varepsilon \cdot \varepsilon_o = 47.32$ μF nm^{-1}.

In this work we considered the four equivalent-circuit models represented in Fig. 1. The circuits shown in Fig. 1a–c implement the components corresponding a single-layer model, whereas the one depicted in Fig. 1d also contains information on the space-charge layer. The circuit depicted in Fig. 1a is the minimal description of an interface with an oxide modelled as a single-layer and yields a single capacitive semicircle: this model is insufficient to follow the experimental data, which typically feature lowered semicircles. The model depicted in Fig. 1b, which contains a CPE, is able to follow this lowering. Figure 1c contains, in addition to the components present in Fig. 1a, also a Gerischer element, accounting for mass transport processes. Finally, the equivalent-circuit of Fig. 1d describes a double-layer oxide with both capacities generalized through a CPE. Non-linear least-squares fits of all data sets were carried out and model selection was performed on the basis of the values of χ^2 and linear correlation coefficient ρ^2 values. We proved that the circuit depicted in Fig. 1b is the soberest one in terms of the parameter space and that it allows a highly accurate description of the experimental data. Briefly, the following reasons suggest to use this simpler model: (i) all qualitative features of the impedance spectra can be captured, (ii) lower confidence intervals for the parameter estimates are obtained, (iii) the parameter estimates are less correlated.

3 Results and discussion

3.1 EIS measurements

In order to evaluate the stability of the *Zr/ZrO$_2$/electrolyte* interface in contact with different aerated electrolytes relevant to dental implant applications, we have kept our samples continuously immersed in the respective solutions and carried out EIS measurements on a discontinuous basis. In particular, we performed three types of exposures and measurements: (A) both exposure and measurements in SBF, (B) both exposure and measurements in SBF with

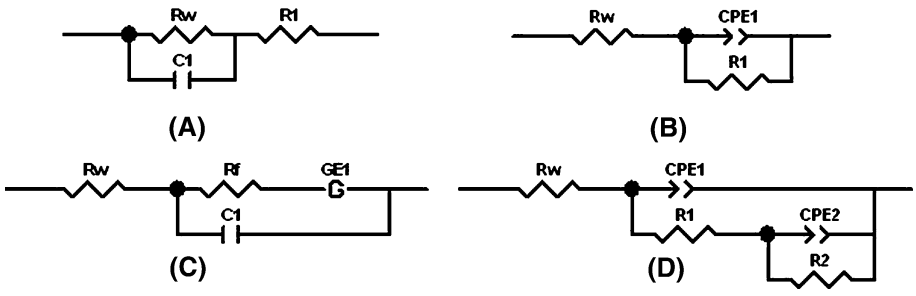

Fig. 1 The equivalent-circuit models selected in this work for the interpretation of the electrochemical impedance spectra reported in Fig. 2

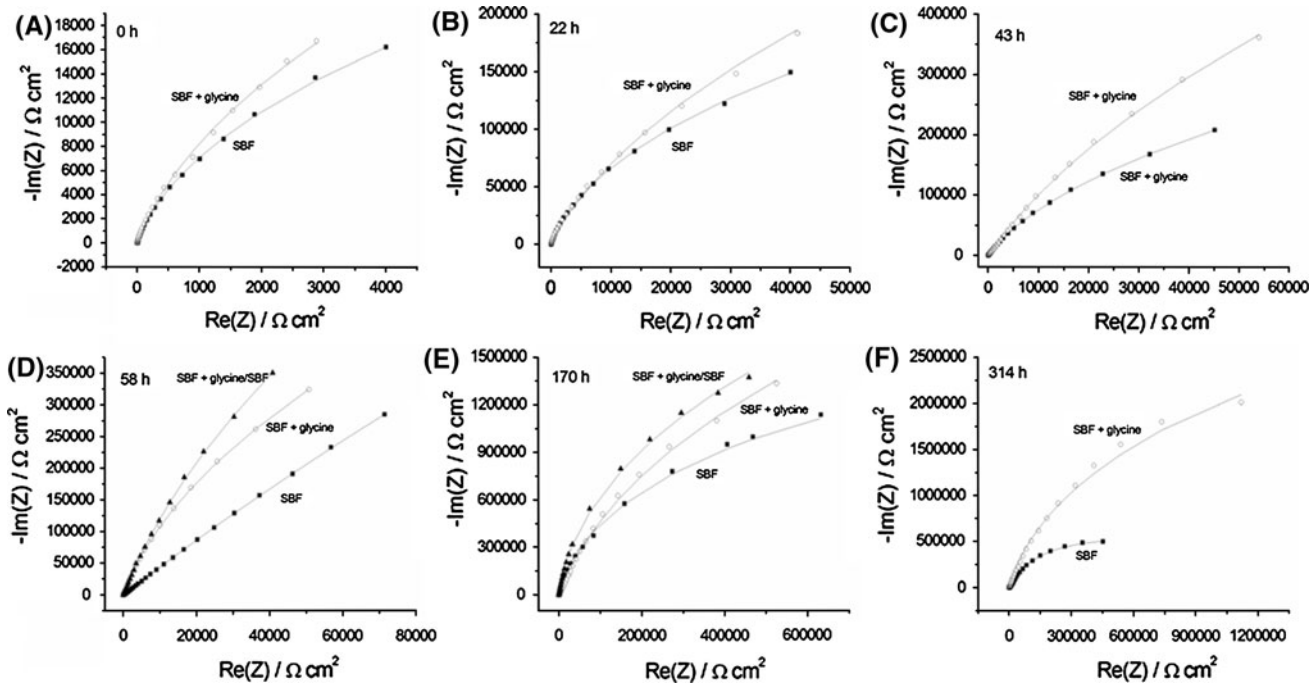

Fig. 2 EIS spectra of Zr in contact with the indicated solutions, measured at open-circuit. *Legend*: "SBF": exposure and measurements in SBF; "SBF + glycine": exposure and measurements in SBF with added glycine; "SBF + glycine/SBF": exposure in SBF with added glycine and measurements in SBF. Spanned frequency range: 65 kHz to 1 MHz, potential modulation: 10 mV

added glycine, (C) exposure in SBF with added glycine and measurements in SBF. In order to check the consistency of results, after each waiting time, three EIS spectra were measured sequentially invariably obtaining negligible differences.

In Fig. 2 we report the experimental EIS results and their fits with the model depicted in Fig. 1b and commented in Sect. 2.2. The fit parameters are reported in Table 1. The estimates of time-dependent passive film resistance, thickness and CPE p-parameter for the systems without and with added glycine, are shown in Fig. 3.

From the EIS results, we can conclude that—in an SBF matrix—in the presence of glycine, appreciably more resistant passivating layers are formed. For the range of immersion times we studied, in fact, in the presence of glycine the film resistance and thickness increase systematically, whereas without glycine these quantities reach a maximum after about 100 h. Furthermore, as one can observe from the time-dependent trend of the CPE p-parameter, in the absence of glycine a rougher film tends to form.

3.2 Characterisation of oxide films

3.2.1 Scanning Electron Microscopy (SEM)

In Fig. 4 we report SEM micrographs of Zr slabs before and after exposure—for 22 and 314 h—to SBF without and with added glycine. Exposure to both solutions leads to a modification of the surface texture, initially showing lamination striations. Exposure to the two investigated solutions initially brings about some degree of smoothing: this effect is more marked with the glycine-containing solution. For prolonged exposures, formation of corrosion product patches as well as localised corrosion features appear: the surface exposed to the glycine-containing electrolyte exhibits a less damaged surface, coherently with the electrochemical measurements discussed in Sect. 3.1.

3.2.2 X-ray diffraction

We studied the crystallographic structure of Zr slabs before and after exposure for 22 h to SBF without and with added glycine. X-ray diffractograms measured at grazing-angle (fixed incidence angle of 0.5°) are shown in Fig. 5. The oxide layers formed under both conditions are so thin that they cannot be detected by XRD, we thus resorted to surface vibrational spectroscopies for their characterisation.

3.2.3 FT-IR reflectance spectroscopy

The FT-IR spectra corresponding to Zr surfaces before and after exposure to SBF without and with added glycine for 170 h are compared in Fig. 6. Zr in pristine conditions exhibits a very small band at ca. 730 cm^{-1}, corresponding to native oxides. Our FT-IR spectra measured after

Table 1 The parameters obtained by non-linear least-squares fits of data reported in Fig. 2 by using the model of Fig. 1b

t (h)	C_p^T	err 95%	C_p^P	err 95%	R_p	err 95%
Exposure and measurements in SBF						
0	3.6355E−5	4.5302E−7	0.9865	0.0030267	94.999	567
22	3.522E−5	5.3392E−7	0.9002	0.0025327	782.009	4.694
43	3.4435E−5	2.847E−7	0.8265	0.0034613	1.652.273	5.352
58	3.295E−5	3.2357E−7	0.80396	0.003124	4.250.474	45.229
170	3.6217E−5	2.847E−7	0.79372	0.0057297	2.963.604	3.281
314	4.0865E−5	1.2776E−6	0.71762	0.0103325	1.000.103	34.576
Exposure and measurements in SBF with added glycine						
0	3.6388E−5	4.3277E−7	0.97849	0.0030107	165.400	5.549
22	3.5396E−5	5.2502E−7	0.97671	0.0018451	1.610.444	16.012
43	2.9664E−5	7.8438E−7	0.94364	0.0024945	3.507.399	19.607
58	2.631E−5	4.4793E−7	0.9419	0.0016585	5.538.908	122.593
170	2.4996E−5	4.6796E−7	0.87942	0.006841	6.196.137	155.183
314	2.1873E−5	5.3271E−7	0.86467	0.005482	7.042.083	113.093
Exposure in SBF with added glycine and measurements in SBF						
58	2.437E−5	3.978E−7	0.9533	0.002142	5.629.439	62.997
170	2.5488E−5	5.125E−7	0.88321	0.003317	6.444.688	159.574

C_p^T and C_p^P are the capacitive term and the exponent of the CPE, R_p is the resistance of the oxide layer, *err 95%* denotes 95% confidence intervals

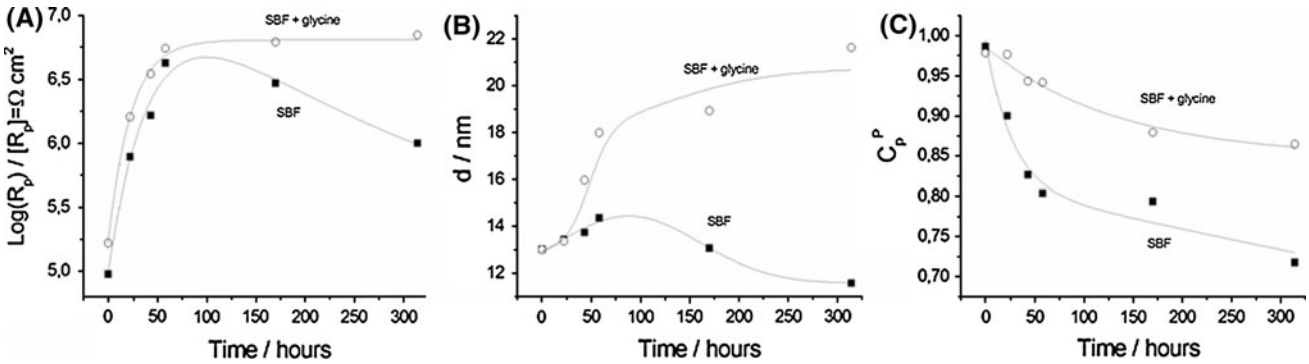

Fig. 3 Non-linear least-squares estimates of time-dependent parameters of EIS measures in SBF without (*squares*) and with added glycine (*open circles*). **a** passive film resistance R_p, **b** passive film thickness d, estimated from the parameter C_p^T, **c** CPA p-parameter C_p^P

immersion in SBF without and with added glydine are essentially the same as those corresponding to phosphated zirconium oxide grown by the sol–gel method [24]. A broad phosphate band derived from the P–O asymmetric stretching mode of the PO_4^{3-} group is found at about 1100 cm^{-1}, denoting incorporation of phosphate in the film [25–28]. In the presence of glycine, this band is shifted to slightly lower wavenumbers. The peaks at 600 and 730 cm^{-1} can be assigned to the O–P–O bending mode [25, 27] and to the Zr–O stretching mode, respectively [29]. In the spectrum corresponding to the surface film formed in the presence of glycine, some weak structure is visible in the range 1350–1650 cm^{-1}, where a sequence of IR peaks of glycine is known to be present (e.g. [30]).

3.2.4 *Surface Raman spectroscopy*

In order to obtain more information on the incorporation of glycine within the ZrO_2 film, we resorted to confocal Raman spectroscopy, exhibiting a higher surface sensitivity with respect to IR. Some weak Raman peaks are found, that enable us to differentiate between oxide films, as shown in Fig. 7. These bands can be interpreted in terms of the following vibrations of glycine (e.g. [31]): 1332 cm^{-1} CH_2 wagging, 1600 cm^{-1} NH_2 scissoring, 2910 cm^{-1} CH stretching. We can thus conclude that the oxide grown in the glycine-containing solution is modified by incorporation of the organic. This modification seems to correlate with a higher corrosion resistance.

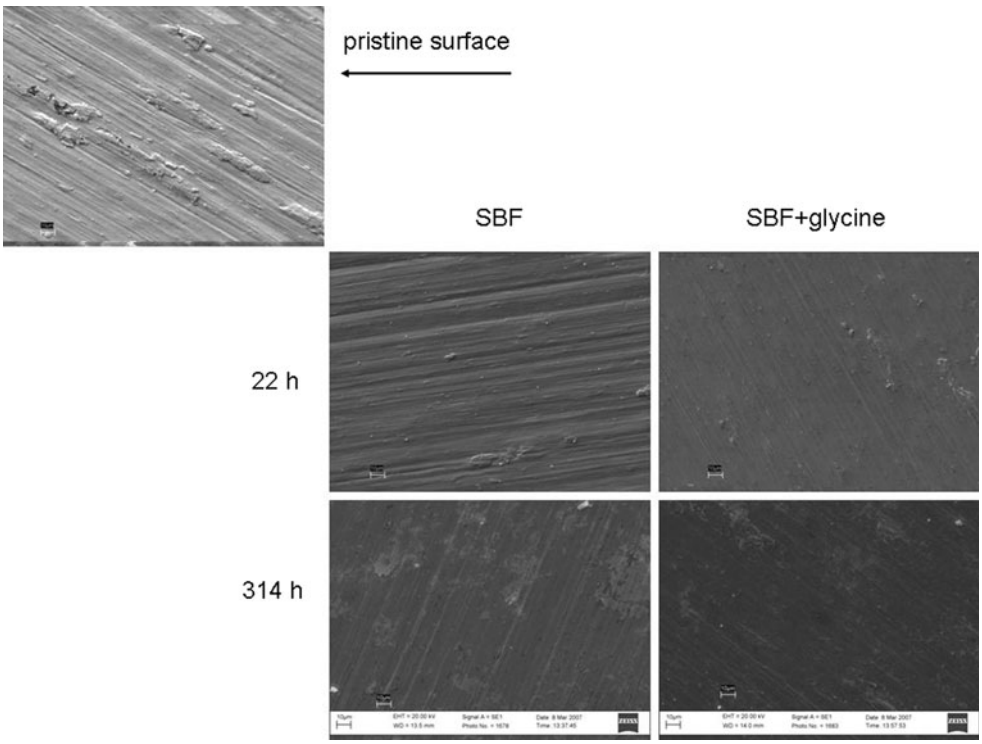

Fig. 4 SEM micrographs of Zr samples before and after exposure—for 22 and 314 h—to SBF without and with added glycine

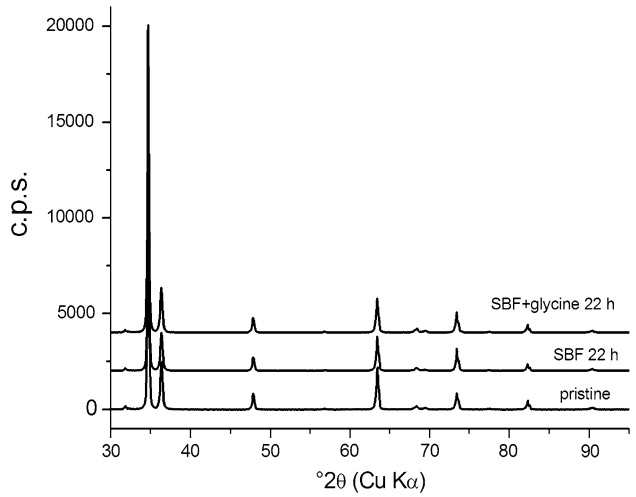

Fig. 5 X-ray diffractograms of Zr samples before and after exposure for 22 h to SBF without and with added glycine

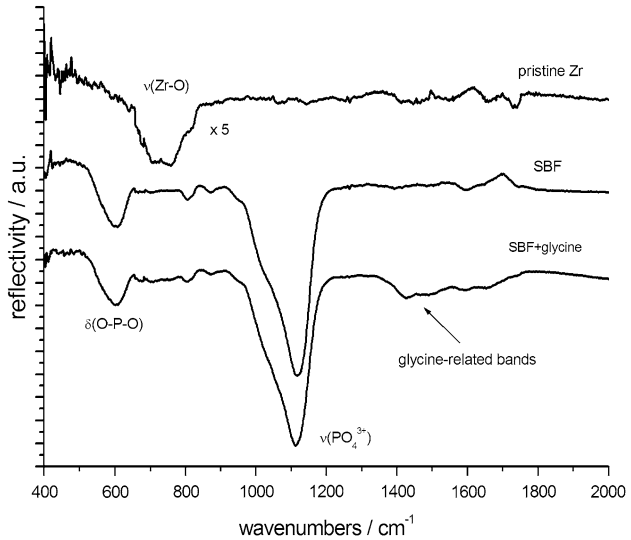

Fig. 6 FT-IR reflectivity spectra of Zr surfaces before and after exposure for 170 h to SBF without and with added glycine

3.2.5 Spectral VIS reflectance

The incorporation of organics into the zirconia layer—leading to modifications of the optical properties—can be independently proved by VIS spectral reflectivity. In particular, the adsorption of organics on ZrO_2 can be highlighted by the increase of VIS spectral reflectivity, as shown in [32] for the case of adsorption of organic intermediates during catalytic isomerisation of alcohols. In Fig. 8 we report the relative reflectivity of Zr samples immersed in SBF without and with glycine addition for 170 h with respect to a Zr sample in pristine condition. The plots refer to averages and standard deviations, derived from sets of three replicate samples for each of the three investigated systems. The reflectivity of samples exposed to the aggressive solution is lower than in the initial condition, owing to both roughening and surface chemical modifications, coherently with the results of SEM and surface vibrational spectroscopies; nevertheless, relatively higher values are found after exposure to the glycine-

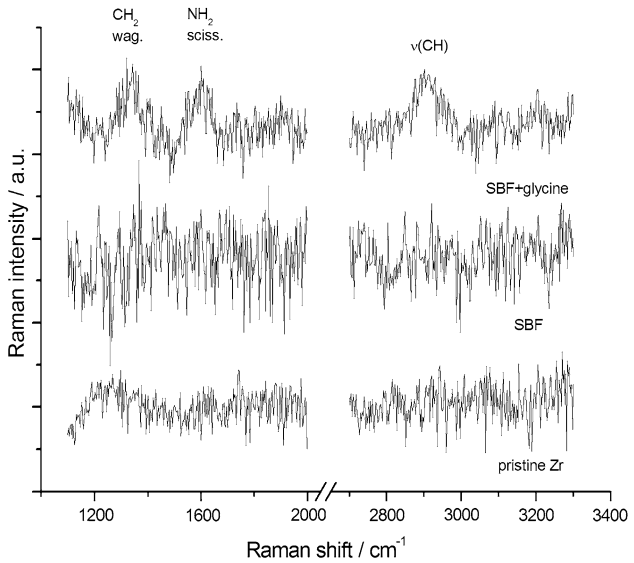

Fig. 7 Surface Raman spectra of Zr surfaces before and after exposure for 170 h to SBF without and with added glycine

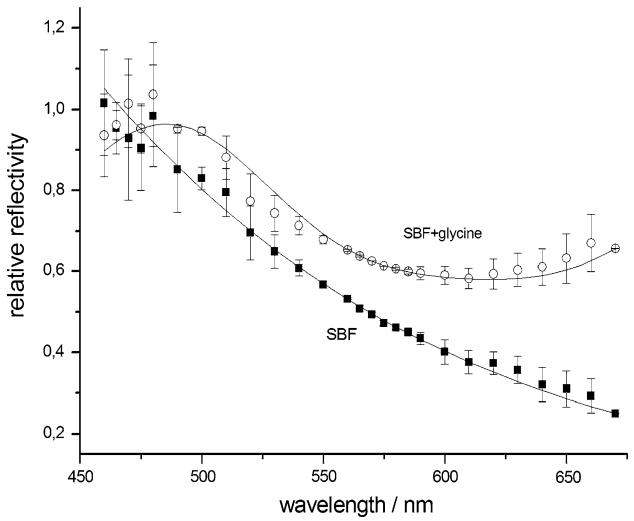

Fig. 8 VIS reflectivity spectra of Zr surfaces after exposure for 170 h to SBF without and with added glycine normalised with the spectrum corresponding to the pristine Zr surface

containing system, possibly denoting both organic absorption and a lower degree of roughening. An insightful interpretation of the wavelength dependence is beyond the scope of the present paper.

4 Conclusions

On the basis of a multi-technique analytical approach, combining electrochemical impedance spectrometry, SEM microscopy, surface vibrational spectroscopies (FT-IR and Raman) and VIS spectral reflectometry, we characterised the surface films forming at the surface of pure Zr exposed to SBF solutions without and with added glycine, as a first step in the simulation of the inorganic and organic components of the implant environment. Electrochemical measurements have shown an outstanding corrosion performance of Zr in both environments, with enhanced protective behaviour corresponding to the presence of glycine. The improved electrochemical behaviour of the oxide film in the presence of the aminoacid correlates with the incorporation of the organic, as proved by surface spectroscopies. The results of this study suggest that the use of surface-oxidised metallic Zr for dental implant applications is likely to offer an improved performance with respect to the cognate Ti technology, based on the combination of the mechanical properties of the metal with the biochemical advantages of a compact and stable surface film of zirconia.

References

1. Bozzini B, Carlino P, D'Urzo L, Pepe V, Mele C, Venturo F. An electrochemical impedance investigation of the behaviour of anodically oxidised titanium in human plasma and cognate fluids, relevant to dental applications. J Mater Sci Mater Med. 2008;19:3443–53.
2. Kobayashi E, Doi H, Yoneyama T, Hamanaka H, Gibson IR, Best SM, Shelton JC, Bonfield W. Influence of aging heat treatment on mechanical properties of biomedical Ti-Zr based ternary alloys containing niobium. J Mater Sci Mater Med. 1998;9:625–30.
3. Tanaka Y, Nakai M, Akahori T, Niinomi M, Tsutsumi Y, Doi H, Hanawa T. Characterization of air-formed surface oxide film on Ti-29Nb-13Ta-4.6Zr alloy surface using XPS and AES. Corros Sci. 2008;50:2111–6.
4. Khan MA, Williams RL, Williams DF. The corrosion behaviour of Ti-6Al-4V, Ti-6Al-7Nb and Ti-13Nb-13Zr in protein solutions. Biomaterials. 1999;20:631–7.
5. Yun YH, Turittu VT, Daigle KP, Kovacs P, Davidson JA, Slack SM. Initial hemocompatibility studies of titanium and zirconium alloys: prekallikrein activation, fibrinogen adsorption, and their correlation with surface electrochemical properties. J Biomed Mater. 1996;32:77–85.
6. Ito A, Okazaki Y, Tateishi T, Ito Y. In vitro biocompatibility, mechanical-properties, and corrosion-resistance of Ti-Zr-Nb-Ta-Pd and Ti-Sn-Nb-Ta-Pd alloys. J Biomed Mater Res. 1995;29:893–9.
7. Kertzman Z, Marchai J, Suarez M, Staia MH, Filip P, Kohli P, Aouadi SM. Mechanical, tribological, and biocompatibility properties of ZrN-Ag nanocomposite films. J Biomed Mater Res A. 2008;84A:1061–7.
8. Okazaki Y, Gotoh E. Implant applications of highly corrosion-resistant Ti-15Zr-4Nb-4Ta alloy. Mater Trans. 2002;43:2943–8.
9. Okazaki Y, Gotoh E. Comparison of metal release from various metallic biomaterials in vitro. Biomaterials. 2005;26:11–21.
10. Okazaki Y. Dental casting properties of Ti-15Zr-4Nb-4Ta alloy. Mater Trans. 2002;43:3134–41.
11. Hendry JA, Pillar RM. The fretting corrosion resistance of PVD surface-modified orthopedic implant alloys. J Biomed Mater Res B. 2001;58:156–66.

12. Eisenbarth E, Velten D, Müller M, Thull R, Breme. Biocompatibility of beta-stabilizing elements of titanium alloys. Biomaterials. 2004;25:5705–13.
13. Ardlin BI, Dahl J, Tibbals JE. Static immersion and irritation tests of dental metal-ceramic alloys. Eur J Oral Sci. 2005;113:83–9.
14. Tsutsumi Y, Nishimura D, Doi H, Nomura N, Hanawa T. Initial hemocompatibility studies of titanium and zirconium alloys: prekallikrein activation, fibrinogen adsorption, and their correlation with surface electrochemical properties. Mater Sci Eng. 2009;C29:1702–8.
15. Godley R, Starosvetsky D, Gotman I. Bonelike apatite formation on niobium metal treated in aqueous NaOH. J Mater Sci Mater Med. 2004;15:1073–7.
16. Aparicio C, Gil FC, Fonseca C, Barbosa M, Planell JA. Corrosion behaviour of commercially pure titanium shot blasted with different materials and sizes of shot particles for dental implant applications. Biomaterials. 2003;23:263–73.
17. Pan J, Thierry D, Leygaf C. Electrochemical impedance spectroscopy study of the passive oxide film on titanium for implant application. Electrochim Acta. 1996;41:1143–53.
18. Hitzig K, Juttner WJ, Lorenz W, Paatsch J. AC-Impedance measurements on corroded porous aluminum-oxide films. J Electrochem Soc. 1986;133:887.
19. Mansfeld F, Kendig MW. Evaluation of anodized aluminum surfaces with electrochemical impedance spectroscopy. J Electrochem Soc. 1988;135:828–33.
20. van Westing EPM, Ferrari GM, de Wit JHW. The determination of coating performance with impedance measurements. 1. Coating polymer properties. Corr Sci. 1993;34:1511–30.
21. Lavos-Valereto IC, Costa I, Wolynec S. The electrochemical behavior of Ti-6Al-7Nb alloy with and without plasma-sprayed hydroxyapatite coating in Hank's solution. J Biomed Mater Res B Appl Biomater. 2002;63:664–70.
22. Bozzini B, Sgura I. A class of mathematical models for alternated-current electrochemical measurements accounting for nonlinear effects. Nonlinear Anal Real World Appl. 2008;9:412–37.
23. González JEG, Mirza-Rosca JC. Study of the corrosion behavior of titanium and some of its alloys for biomedical and dental implant applications. J Electroanal Chem. 1999;471:109–15.
24. Wong MS, Antonelli DM, Ying JY. Synthesis and characterization of phosphated mesoporous zirconium oxide. Nanostruct Mater. 1997;9:165–8.
25. Colthup NB, Daly LH. Introduction to infrared and Raman spectroscopy. San Diego: Academic Press, Inc.; 1990. p. 363–6.
26. Iwasita T, Nart FC. In-situ infrared Fourier transform spectroscopy: a tool to characterize the metal-electrolyte interface at a molecular level. In: Gerischer H, Tobias CW, editors. Advances in electrochemical science and engineering, vol 4. Weinheim: VCH; 1995. p. 169–71.
27. Nakamoto K. Infrared and Raman spectra of inorganic and coordination compounds. New York: Wiley; 1997. p. 266.
28. Müller L, Müller FA. Preparation of SBF with different HCO_3^- content and its influence on the composition of biomimetic apatites. Acta Biomater. 2006;2:181–9.
29. Ghosh A, Suri AK, Pandey M, Thomas S, Rama Mohan TR, Rao BT. Nanocrystalline zirconia-yttria system—a Raman study. Mater Lett. 2006;60:1170–3.
30. Fischer G, Cao X, Cox N, Francis M. The FT-IR spectra of glycine and glycylglycine zwitterions isolated in alkali halide matrices. Chem Phys. 2005;313:39–49.
31. De Gelder J, De Gussem K, Vandenbeele P, Moens L. Reference database of Raman spectra of biological molecules. J Raman Spectrosc. 2007;38:1133–47.
32. Ahmad R, Melsheimer J, Jentoft FC, Schlögl R. Isomerization of n-butane and of n-pentane in the presence of sulfated zirconia: formation of surface deposits investigated by in situ UV-vis diffuse reflectance spectroscopy. J Catal. 2003;218:365–74.